

# NUMERICAL INVESTIGATION OF A HYBRID MECHANICAL-ADHESIVE JOINING TECHNOLOGY FOR APPLICATION IN LIGHTWEIGHT COMPOSITE-METAL STRUCTURES

Michael C. Corbett<sup>1</sup> and Conor T. McCarthy<sup>1</sup>

<sup>1</sup> Irish Composites Centre (IComp), Bernal Institute, School of Engineering, University of Limerick, Limerick, Ireland, <http://www.falcom.ie>

**Keywords:** Continuum damage model, Cohesive zone model, Joints, Hybrid structures, Finite elements

## ABSTRACT

A novel concept for the structural joining of composite and metallic components is presented. The concept employs interlocking morphology formed on the surfaces of composite, female and metallic, male adherends that are coupled with a layer of adhesive so that they mechanically interlock in shear. In the present work, miniature, single-lap adhesive joint specimens are considered, with a single truncated square pyramid interlocking profile, centred in the bond area. Finite element (FE) models of the interlocking joint architecture are developed in order to assess the mechanical performance of the concept. The modelling approach incorporates an intralaminar continuum damage model to account for damage in the composite material, a cohesive zone damage model to represent damage and fracture propagating through the adhesive, and elastic-plastic behaviour to simulate the mechanical response of the metal. The model is validated against experimental results, showing good correlation in terms of stiffness, strength and damage predictions. The concept demonstrates improvements of up to 18.3% in terms of the joints ultimate failure load when compared to a standard adhesively bonded joint. Importantly, significant improvements in the work required to break the joint have also been demonstrated, with up to 41% shown in simulations. The improvement in work to failure is achieved through the more progressive way that the interlocking joint fails when compared to a standard adhesive joint. This is achieved as a result of the mechanical interlock, which prevents sudden catastrophic failure caused by the adhesive but instead leads shear-out and net-tension failure modes, which are typical of bolted joints.

## 1. INTRODUCTION

Joining composites to metals is a key enabling technology that will help to drive the integration of future hybrid, composite-metal, structures. The current industry standard for joining in these structures depends on mechanical fastening and adhesive bonding. These techniques have undergone substantial development in the past number of decades and hence, are approaching the upper limit of their potential performance. Despite this, each technology still presents inherent weaknesses. Mechanical fastening is inefficient; it adds weight and introduces stress concentrations to the structure. Adhesive bonding provides improved efficiency but presents difficulty in achieving consistent strength, which affects reliability and leads to the over-design of structures. Recently, a number of hybrid joining processes have emerged which combine the positive traits of the fundamental techniques; such as weld-bonded and bonded-bolted joints. In the present work, a novel, hybrid mechanical-adhesive joining concept is explored. The concept is based on the fact that the central overlap region of an adhesively bonded joint is relatively inactive for load transfer. In order to activate this area, interlocking profiles are formed on the surfaces of male (metallic) and female (composite) adherends and coupled with a layer of adhesive. Thus, the hybrid joint provides the mechanical interlocking and added reliability of mechanical fastening together with the efficiency of bonding; without a weight penalty.

The concept has previously been investigated through finite element (FE) analysis and optimised by

the present authors [1], for an interlocking joint with metallic male and female adherends. The results demonstrated impressive improvements in both the joint's ultimate failure load and the work required for fracture. Herein, the concept is investigated through three-dimensional finite element analysis of the joint architecture in a hybrid, composite-metal joint configuration. Sophisticated material models are employed in order to simulate deformation and damage of the composite, adhesive and metal; making it possible to accurately capture the mechanical response of the joint until catastrophic failure. Thus, it is possible to explore the role of the interlocking geometry on stress distribution within the adhesive, and on crack propagation and arrest after initial fracture. The current work presents the validation of the proposed FE model against results from an associated experimental investigation, with the aspiration that the FE model may be used to optimise the hybrid joining concept numerically.

## 2. PROBLEM DESCRIPTION

The subject of the present investigation is a hybrid, composite-metal, miniature adhesively bonded single-lap joint (SLJ), as shown in Figure 1a. This specimen geometry was chosen corresponding to the analogous experimental investigation, as it allows for in-situ testing within an SEM chamber [2]. The joint's interlocking morphology is represented in its most fundamental form, as a single truncated square pyramid profile, centred in the 35mm<sup>2</sup> joint overlap area. This allows for effective investigation of the performance of the concept and the deformation and damage mechanisms occurring around a single profile. The design of this geometry may be described by four factors; length ( $X_1$ ), depth ( $X_2$ ), width ( $X_3$ ), and inclination angle ( $X_4$ ), which are based on the female adherend, as shown in Figure 1b.

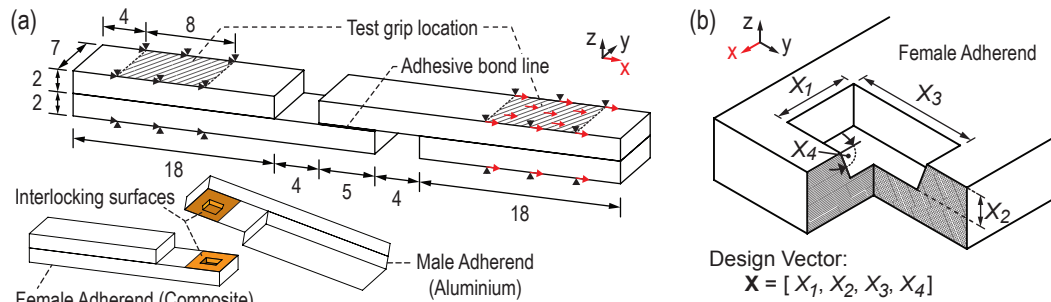


Figure 1: Miniature interlocking SLJ (a) geometry and boundary conditions (dimensions in millimetres) and (b) truncated, square pyramid interlocking profile geometry and corresponding geometric factors.

The female adherend is characterised by a depression in its surface corresponding to the interlocking morphology and was manufactured from a carbon fibre/epoxy matrix system, HTA/ 6376. Each lamina has a nominal thickness of 0.125 mm. Thus, the resulting laminate had 16 plies, stacked in a quasi-isotropic configuration,  $[0/0/90/90]_{2s}$ . The depression in the surface of the female adherend was manufactured through a laser machining process similar to that adopted by Leone et al. [3]. A representative experimental specimen is shown in Figure 2. The male adherend is distinguished by a protruding interlocking profile which is defined to fit the female adherend, with a constant clearance of 55  $\mu\text{m}$ . It is machined from an aluminium alloy, AA5754 [4]. Both adherends are coupled with a constant thickness adhesive layer, which fills the 55  $\mu\text{m}$  [2] clearance space between the interlocking surfaces. The adhesive system employed is a bi-component structural epoxy resin, Loctite<sup>®</sup> Hysol 9466 [5]. There were four miniature adhesively bonded joint configurations tested during the associated experimental investigation, three interlocking examples and a corresponding, baseline (E0), standard adhesively bonded joint. The geometry of the interlocking joints is described per Table 1, comprising of a rectangular interlocking profile, which is longer in the loading direction (E1), a profile which is longer transverse to the loading direction (E2), and a smaller, square profile (E3). These designs were set out to compare the performance of three diverse interlocking designs. The specimens are compared to the baseline in each case in order to distinguish improvement in performance for the interlocking adhesive joint concept.

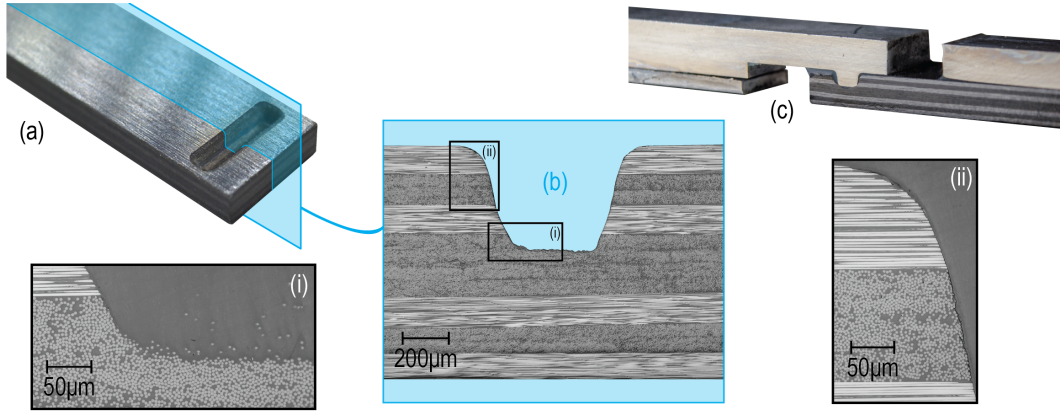


Figure 2: Interlocking miniature adhesive joint specimen employed during experimental trials; (a) laser-machined, composite, female adherend, (b) microscopy of the cross-sectioned composite, female adherend, and (c) bonded and cross-sectioned test specimen.

Table 1: Description of the interlocking morphology of the experimental specimens.

Joint	$X_1$ [mm]	$X_2$ [mm]	$X_3$ [mm]	$X_4$ [°]
$E0^*$	-	-	-	-
$E1$	3.0	0.75 <sup>†</sup>	1.2	85.0
$E2$	1.2	0.75 <sup>†</sup>	5.5	85.0
$E3$	1.5	0.75 <sup>†</sup>	1.5	85.0

\* Standard miniature adhesive joint.

<sup>†</sup> Equivalent to 6 ply thicknesses.

### 3. FINITE ELEMENT MODEL

A miniature adhesive joint model was developed in the commercial FE software, Abaqus<sup>®</sup> [6]. The model was composed of separate parts for the male and female adherends. The adhesive was represented by a solid orphan mesh, offset from the bond surface of the female adherend. During analysis, the parts were tied together with surface based tie constraints [6]. The parts were idealised in order to facilitate meshing; machining fillets, which were present in the experimental specimens, were excluded and the joint was modelled with no adhesive fillet. Model creation and meshing were automated through a Python<sup>™</sup> script. Global and local nodal seeds were appropriately assigned such that mesh density was increased at the ends of the joint overlap, where large gradients in strain localise and in the vicinity of the interlocking profile, in order to accurately capture deformation of the composite material.

The response of the metallic, male adherend was characterised by elastic-plastic behaviour, incorporating von Mises yield criteria and isotropic strain hardening defined through Holloman's equation (Eq. 1). The stress-strain response of AA5754 was produced from experiments; salient mechanical properties are summarised in Table 2. This material was represented by 8-node, linear, brick elements with reduced integration and hourglass control (C3D8R) [6]. No damage model was implemented in the metallic material as it was assumed that damage would develop in the composite adherend or cohesive failure would occur prior to failure of the aluminium.

$$\sigma = K \varepsilon_p^n \quad (1)$$

where  $\sigma$  is the true stress,  $K$  is the strength coefficient,  $\varepsilon_p$  is the true plastic strain and  $n$  is the strain hardening exponent.

The composite, female adherend was represented by a layered model, incorporating each lamina as an orthotropic material, accounting for the variation in stiffness through the thickness of the adherend. Each

lamina was represented by a single layer of 8-node, linear, brick elements with reduced integration and hourglass control (C3D8R) [6]. The mechanical response of this material was represented by an intralaminar continuum damage model (CDM); allowing for the simulations to accurately reflect the damage mechanisms occurring during experiments. A description of this model is provided per Section 3.1.

Table 2: Mechanical properties of the aluminium alloy, AA5754 [4].

$E(GPa)$	$\nu$	$\sigma_y(MPa)$	$K(MPa)$	$n$	$\sigma_{uts}(MPa)$
68	0.33	110	360.1	0.194	299.58

There were two approaches adopted to model the adhesive layer. In order to analyse deformation and stress in the adhesive prior to the onset of damage, it was represented by an elastic-plastic constitutive model. Similar high-strength, two-part epoxy adhesive systems to that employed herein have been shown to exhibit dependence of yield on hydrostatic stress [7]. The Mohr-Coulomb yield criterion has been applied in order to capture this behaviour. The friction angle,  $\phi$ , which determines the influence of normal stress on the yielding behaviour of the material, and the cohesion yield stress,  $c$  were assigned similarly to O'Dwyer et al. [7]. Correspondingly, non-associated flow was assumed, and the angle of dilation was set to zero. The mechanical properties of the adhesive system are summarised in Table 3. This material was discretised by 8-node, linear, brick elements with reduced integration and hourglass control (C3D8R) [6], with six elements through the thickness of the adhesive. Subsequently, a cohesive zone damage model (CZDM) was employed to simulate the propagation of damage and fracture in the adhesive. In these models, the adhesive was represented, with its true thickness, by a single layer of 8-node cohesive elements (COH3D8) [6]. Details of the CZDM formulation are presented in Section 3.2. By applying the CZDM in combination with the composite CDM, it was possible to accurately represent the mechanical response of the interlocking joints until catastrophic failure of the joint. Implicit simulations were conducted with the large strain formulation, NLGEOM [6], and the specimen was loaded in quasi-static, displacement controlled tension from the grip locations shown in Figure 1a.

Table 3: Mechanical properties of the adhesive, Hysol 9466 [5, 7].

$E(GPa)$	$G(MPa)$	$\nu$	$\sigma_{uts}(MPa)$	$c(MPa)$	$\phi$
1.718	636.6	0.35	32	30	15°

### 3.1 Composite Damage Model

In order to accurately represent deformation and failure occurring in the composite adherend, a physically based damage model was employed. The basic formulation of this model was originally developed by Ladeveze & Le Dantec [8]. for the prediction of transverse and shear damage in composite plies. This model was extended to three dimensions, with shell elements, by Frizzell et al. [9]. Zhou et al. [10] subsequently developed this model for solid, brick elements and incorporated a number of enhancements for the simulation of composite bolted joints. A brief overview of the model is presented here.

At the ply level, damage is assumed to take the form of matrix micro-cracking, fibre-matrix debonding and fibre fracture. The model includes the effect of shear-transverse behaviour coupling and plasticity, to account for irreversible strains in undamaged parts of the matrix, and incorporates non-linear in-plane shear behaviour. The Hashin criteria [11] is employed to predict tensile and compressive fibre failures, while the crack band model [12] is used to mitigate mesh sensitivity. Puck's criteria [13] is incorporated in order to predict intralaminar damage by checking for damage initiation on multiple potential fracture planes. This provides a rational approach to the degradation of material stiffness depending on whether failure is similar to delamination, transverse cracking, or mixed mode. Although this does not explicitly consider interlaminar damage, it is a highly efficient way to include the effects of transverse damage, similar to delamination, without resorting to the application computationally expen-

sive cohesive elements at each ply boundary.

This material model was implemented in an Abaqus<sup>®</sup> UMAT subroutine [6]. A more thorough explanation of the implementation has been presented by Zhou et al. [10]. O'Higgins [14] carried out a number of statistically robust experimental tests to determine the material properties and describe the damage development laws of HTA/6376. The elastic and damage development law properties employed are presented in Tables 4 & 5 respectively. The maximum value of the damage variable,  $d^{max}$  was set to 0.95; this enforced a minimum element stiffness which ensured numerical stability, as deletion of three-dimensional stress elements is not supported for implicit analyses in Abaqus<sup>®</sup>.

Table 4: Elastic properties of the composite material, HTA/6376 [14].

$E_{11}(GPa)$	$E_{22}(GPa)$	$E_{33}(GPa)$	$G_{12}(GPa)$	$G_{13}(GPa)$	$G_{23}(GPa)$	$\nu_{12}$	$\nu_{13}$	$\nu_{23}$
139.3	10.14	10.14	6.02	6.02	3.9	0.32	0.32	0.5

Table 5: CDM properties of the composite material, HTA/6376 [14].

$X_T(MPa)$	$X_C(MPa)$	$Y_T(MPa)$	$Y_C(MPa)$	$S_{12}(MPa)$	$S_{13}(MPa)$	$a$	$b$
2170	1600	70	250	82.62	120	0.397	0.493
$Y_{12_0}(\sqrt{Pa})$	$Y_{12_c}(\sqrt{Pa})$	$Y_{22_0}(\sqrt{Pa})$	$Y_{22_c}(\sqrt{Pa})$	$R_0(MPa)$	$\beta(MPa)$	$\mu$	
48	3000	100	3100	21.59	512.9	0.41	

### 3.2 Cohesive Zone Damage Model

A mixed-mode CZDM was adopted in consideration of both normal (mode I) and tangential (mode II & III) deformation and damage within the adhesive layer. The model is implemented in Abaqus<sup>®</sup> 6.14 [6]. In each mode the response of these elements obey a bi-linear traction-separation law with linear softening. The initial stiffness of the cohesive elements is governed by the elastic properties of the adhesive. Interaction between each mode of loading during damage initiation is accounted for according to the quadratic stress criterion, as per Eq. 2. This rule has previously achieved excellent agreement to experimental tests of adhesive joints [15].

$$\left(\frac{\langle t_n \rangle}{t_n^o}\right)^2 + \left(\frac{t_s}{t_s^o}\right)^2 + \left(\frac{t_t}{t_t^o}\right)^2 = 1 \quad (2)$$

where  $t_n$ ,  $t_s$  and  $t_t$  represent the normal, in-plane tangential and out-of-plane tangential tractions respectively, and  $t_n^o$ ,  $t_s^o$  and  $t_t^o$  are the critical traction values in each mode.

Once damage has initiated, the stiffness of the cohesive elements softens progressively according to a damage parameter,  $D$ , which monotonically evolves from 0 to 1 upon further loading after damage initiation. Damage evolution is controlled by the linear fracture energetic criterion, according to Eq. 3, as similarly applied to adhesive joints by numerous authors [15]. Once this criterion is satisfied  $D$  is set to 1, the element may no longer carry load and is deleted from the model thus allowing fracture to propagate.

$$\left(\frac{G_n}{G_n^C}\right)^\alpha + \left(\frac{G_s}{G_s^C}\right)^\alpha + \left(\frac{G_t}{G_t^C}\right)^\alpha = 1 \quad (3)$$

where  $G_n$ ,  $G_s$  and  $G_t$  represent the normal, in-plane tangential and out-of-plane tangential fracture energy release rates respectively,  $G_n^C$ ,  $G_s^C$  and  $G_t^C$  are the critical fracture energies in each mode, and  $\alpha = 1$  for the linear fracture energetic criterion.

The properties of the CZDM were determined through an inverse calibration procedure. The tangential, mode II and mode III properties were assumed to be equal to one another, i.e.  $t_s^o = t_t^o$ , and

$G_s^C = G_t^C$ . The associated material properties are outlined in Table 6.

Table 6: Cohesive zone model properties of the adhesive, Hysol 9466.

$t_n^o$ (MPa)	$t_s^o$ (MPa)	$G_n^C$ (J/m <sup>2</sup> )	$G_s^C$ (J/m <sup>2</sup> )
32.8	18.6	0.44	0.687

#### 4. RESULTS & DISCUSSION

The results of the experimental test specimens, E0 to E3 are compared to corresponding simulations, labelled S0 to S3. The mechanical response of the simulated interlocking joints is compared to that of representative experimental specimens in Figure 3. The stiffness and strength of the simulations correspond well to that of the experiments for each configuration. The interlocking joints present an improvement in ultimate failure load compared to the standard joint; the most significant improvement being from configuration 1. The magnitude of this increase is 18.3% based on the mean experimental results and 11.2% based on the corresponding simulations. The stress distribution in the adhesive layer prior to damage propagation is considered in Section 4.1 in order to establish an understanding of the mechanics governing deformation and initial failure of the interlocking adhesive joints. The damage tolerance of the concept will be discussed in Section 4.2

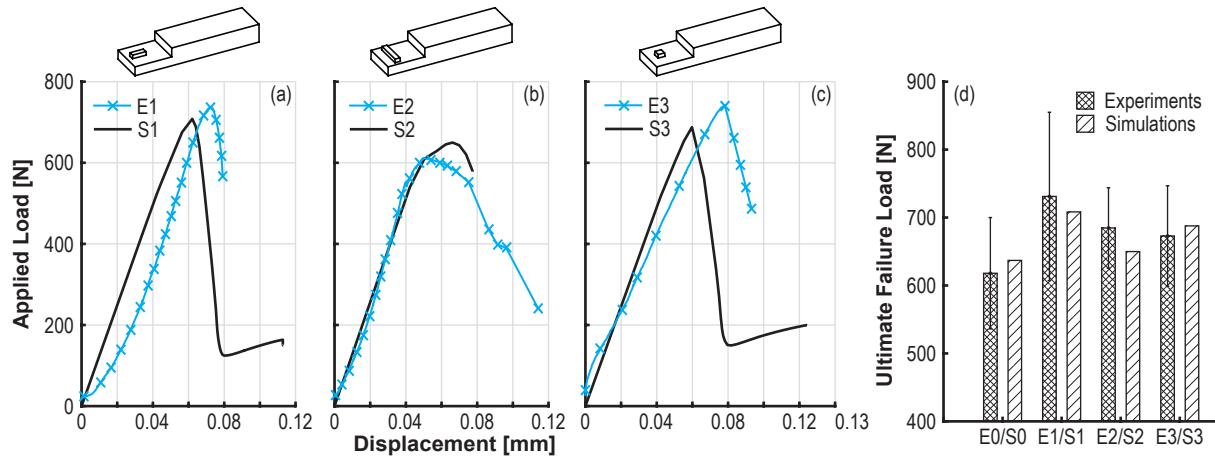


Figure 3: Mechanical response of simulated interlocking joints, S1, S2, and S3 compared to that of representative experimental specimens, E1, E2, and E3; and the ultimate failure loads of the simulations compared to experimental results for each configuration.

##### 4.1 Adhesive Stress Distribution

The adhesive was modelled as an elastic-plastic material, as per Section 3. A constant load,  $F$  was applied to the joint; two load levels were considered: 250N and 625N. These loads corresponded to linear and non-linear deformation of the joint respectively, the latter being just prior to damage propagation as determined from experimental tests. The stress distributions were extracted from a surface at the centre of the adhesive thickness. Interlocking joint configuration 1 is compared to a standard adhesively bonded joint. The normal and tangential adhesive stress distributions in a symmetrical half of the interlocking joint's overlap, for a load of 250N, are presented in Figure 4. The stress distributions in a path at the  $x$ - $z$  mid-plane of the interlocking joint are compared to that of the standard joint in Figure 5; in which both load levels are considered. In order to discuss the influence of the interlocking morphology, the joint overlap region is described by its female end, i.e. the end of the bond closest to the constraint of the female (composite) adherend, and vice versa, its male end. The cutaway cross-sectional profiles of each adhesive layer are also provided above Figure 5 for clarity.

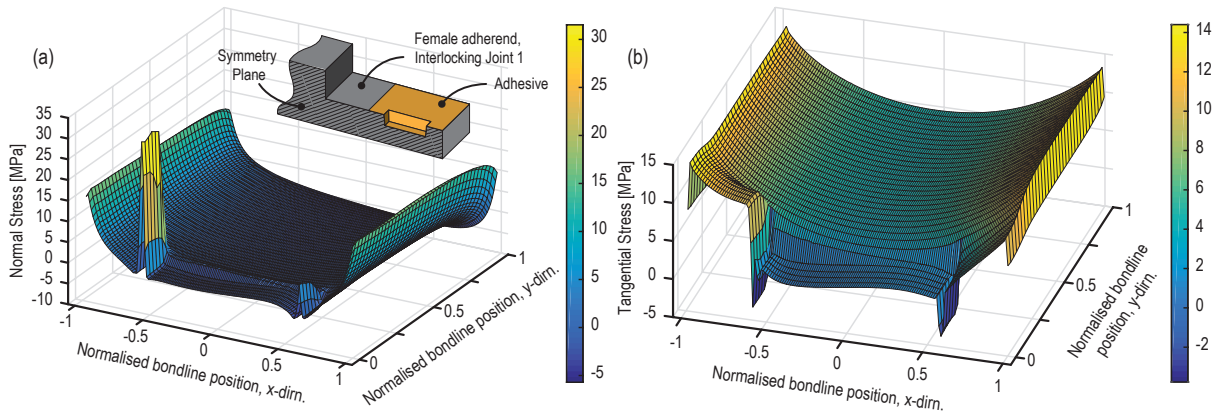


Figure 4: Normal (a) and tangential (b) stress distributions in a symmetrical half of the overlap of interlocking joint E1, loaded to 250N.

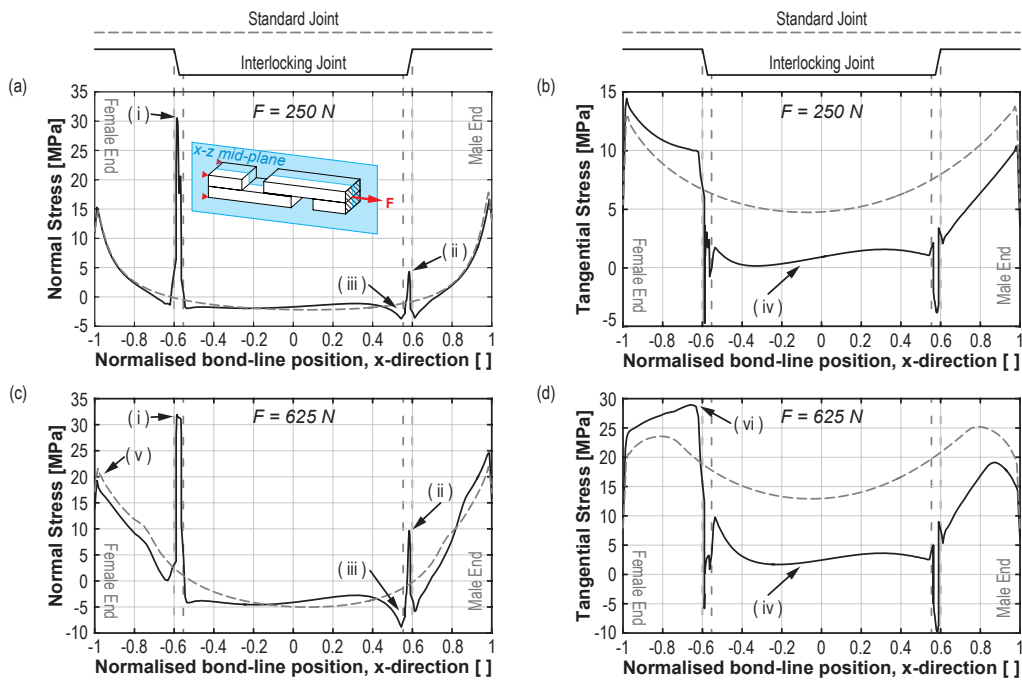


Figure 5: Normal (a,c) and tangential (b,d) adhesive stress distributions in a path at the x-z mid-plane of the interlocking and the standard joints, for loads of 250N (a,b) and 625N (c,d).

Considering elastic deformation of the joint ( $F=250\text{N}$ ), the normal stress distribution in the adhesive (Figure 5(a)) demonstrates concentrations at the ends of the joint overlap, with minimal difference between the interlocking and standard joints. However, in the interlocking joint there are also peaks in normal stress on the faces of the interlocking profile near both the female and male ends of the bond (i & ii); the peak at the female end (i) being greater as a result of the loading direction. This indicates that the mechanical interlock is relatively inactive for load transfer while the joint deforms elastically. However, there is also an increase in compressive normal stress along the base of the interlocking profile (iii). The remainder of the bond area shows a similar stress distribution to that of the baseline joint. In terms of the tangential stress distribution (Figure 5(b)), differences between the interlocking and standard joints in the vicinity of the interlocking profile are more apparent. There is minimal stress in the adhesive along the base of the interlocking profile (iv). While tangential stress at the female and male ends of the bond, around the profile, are increased and decreased respectively, compared to the standard joint.

During non-linear deformation of the joint ( $F=625\text{N}$ ), the stress distribution in the adhesive evolves

considerably. Normal stress in the adhesive (Figure 5(c)) at the profile face at the female end of the bond (i) has reached the tensile strength of the adhesive, indicating that failure would initiate in this region. Compressive normal stress at the base of the profile (iii) has increased. Interestingly, normal stress at the female end of the bond (v) is less than that of the standard joint; although the opposite is true at the male end. This may contribute to the fact the interlocking joint attained a greater ultimate failure load than the standard joint, as fracture initiated from the female end of the bond. In consideration of the tangential stress distribution (Figure 5(d)), as a result of plastic deformation of the adhesive at the ends of the joint overlap, the peak in shear stress moved towards the centre of the bond as the load increased (for both the interlocking and standard joints). However, for the interlocking joint, tangential stress at the female end of the bond (vi) remains considerably greater than that at the male end. As a result, plasticisation of the adhesive at the female of the bond is more significant and the peak in stress has moved further, approaching the face of the interlocking profile. This indicates that failure occurs when this peak in tangential stress reaches the face of the profile, where there is a concentration in normal stress.

#### 4.2 Progressive Damage Analysis

The mechanical response and failure of interlocking joint configurations 1 and 3 were similar. During experiments fracture initiated in the adhesive at the female end of the joint overlap and subsequently at the male end before propagating rapidly across the adhesive bond. At this point the male and female adherends popped out of their interlocked position as a result of insufficient lateral constraint and possibly due to elastic snap-back from the mechanical grips, given the sudden, large drop in load indicated by the simulation. In contrast to this, for configuration 2, damage also initiated in the adhesive at the female end of the overlap but the joint experienced similar to net-tension type failure in the composite adherend. Similar behaviour was observed in the simulation, which showed unstable mechanical response prior to achieving its ultimate failure load, which was correspondingly reduced (Figure 3). The simulation of interlocking joint configuration 1 will be considered in further detail and compared to the experiment herein. The analysis of the other configurations remains for future work.

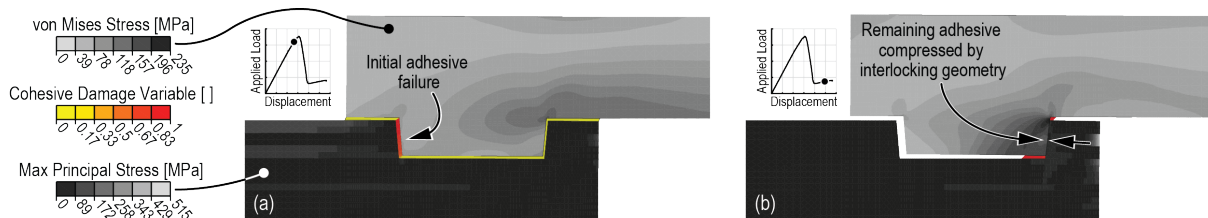


Figure 6: Contour plots of interlocking joint S1, (a) prior to achieving its maximum applied load and (b) prior to ultimate failure of the joint.

It was observed from the simulation (S1) that, in fact, the adhesive on the profile face at the female end of the bond failed before the adhesive at the ends of the joint overlap, as similarly indicated by the adhesive stress analysis, per Section 4.1 and illustrated in Figure 6a. Nevertheless, failure of the adhesive at the female end of the joint overlap governed the ultimate failure load of the joint. The simulated joint experienced a significant reduction in load subsequent to achieving its maximum load. However, in contrast to the experiment, the joint remained intact. At this point fracture had propagated throughout most of the adhesive, with the exception of the region at the profile face at the male end of the overlap, in which compressive stresses were induced on the adhesive which arrested fracture from propagating and allowed for the joint to sustain further loading, as in Figure 6b.

As the applied load on the joint increased once again, the composite adherend was subjected to significant matrix damage, because all of the load carried by the joint was transferred through the mechanical interlock between the composite and metallic adherends. The development of damage in the simulated composite adherend is illustrated in Figure 7, where matrix damage is shown sequentially at various ply

depths. Four load levels are shown, corresponding to columns (a) - (d). It was observed that matrix damage began to develop, in line with the edge of the interlocking profile, in the loading (x) direction, as the joint achieved its maximum load (column (a), Figure 7). A similar matrix crack was observed in an experimental specimen, spanning two zero degree plies in depth. Although damage sustained by the composite adherend (E1) during the experiment was not apparent through visual inspection, an xradia<sup>®</sup> Versa XRM-500 x-ray microscope was employed to achieve three-dimensional x-ray images of a specimen. Inspection of these images revealed matrix cracking and delamination of the composite, as shown in Figure 8.

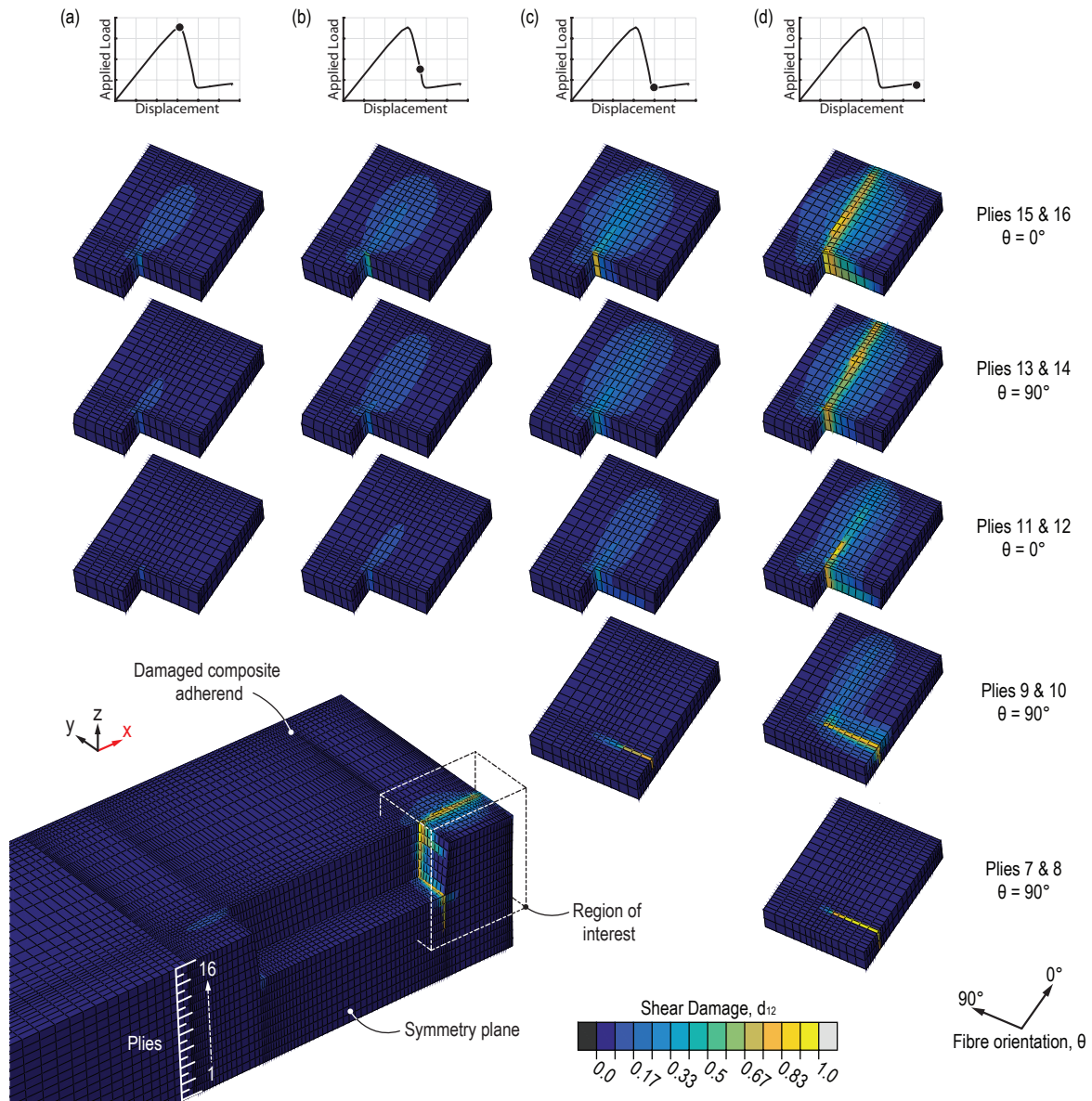


Figure 7: Development of damage in each composite ply for interlocking joint configuration 1 (S1) during various stages of loading.

These images reveal that matrix damage observed in the experimental specimen was predicted accurately. However, a symmetrical crack, propagating from the opposite edge of the interlocking profile was not apparent in the experimental specimen. This may have been a result of alignment of the adherends during bonding or loading. The delamination observed in the experimental specimen, equal in width to the interlocking profile and propagating from near to the end of the profile to the end of the adherend between layers of 90° and 0° plies, was not apparent from the simulation. This is a deficiency of the

composite CDM, as it is not formulated to explicitly account for interlaminar damage.

Upon further loading (columns (c) and (d), Figure 7), which, as previously discussed, was not demonstrated by the experiment, the simulation indicated that the composite adherend would exhibit shear-out type failure, developing from the matrix crack observed experimentally. Matrix damage also subsequently occurred in the 90°plies at the base of the interlocking profile (plies 7-10). This damage propagated perpendicular to the loading direction. Similar matrix damage was noted, occurring in these plies, for experiments conducted on interlocking joint configuration 2; highlighting that the present laminate stacking sequence may be ineffective for the interlocking adhesive joint concept. There was no fibre damage apparent from either the simulation or the experimental specimens. The progressive failure phenomena demonstrated by the interlocking joint resulted in an improvement in work to fracture (energy required to break the joint) of 41.5% compared to the standard adhesive joint simulation.

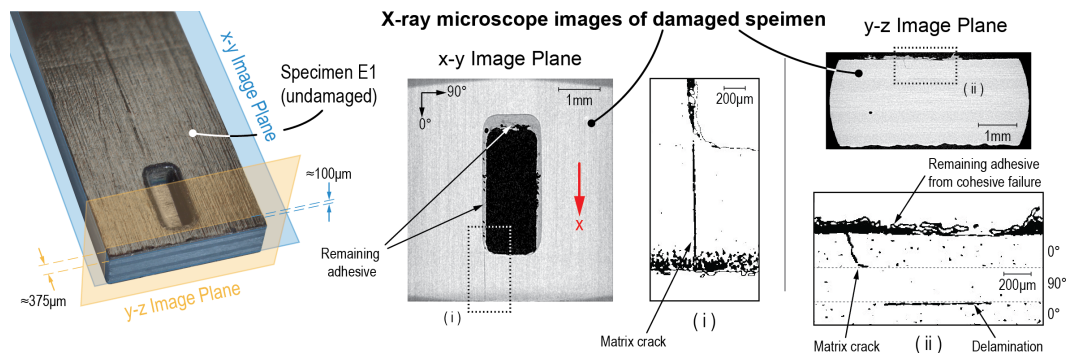


Figure 8: X-ray microscope images of the female, composite adherend of experimental specimen E1, revealing matrix cracking and delamination.

## 5. CONCLUSIONS

The mechanical response of the interlocking adhesive joint concept has been investigated thoroughly through finite element analysis. It has been shown that the concept may present improvements in ultimate failure load of up to 18.3% when compared to a standard adhesively bonded joint. This improvement is brought about by the way stress in the adhesive develops in the interlocking joint during non-linear deformation. It has been shown that, just prior to fracture, the normal stress in the adhesive is of the interlocking joint is less than that of the standard joint at the end of the overlap at which fracture occurs, delaying the propagation of fracture through the adhesive.

In addition, the concept presents a more progressive failure process with the potential to absorb much more energy (up to 41.5%) than a standard adhesive joint during fracture. These are significant developments given that a primary weakness of the adhesive joint is the rapid *un-zipping* of the adhesive bond during failure. The results presented herein demonstrate the capability of the finite element model which has been presented to reproduce the mechanical response, determined experimentally, of the interlocking adhesive joint. In addition, it has been shown that the model accurately simulates the progression of damage in the composite adherend resulting in failure of the joint. As a result, this model will be used to explore alternative interlocking geometries in order to optimise the performance of the concept; which should subsequently feed back to the ongoing experimental investigation.

## ACKNOWLEDGEMENTS

The authors acknowledge the financial support of Science Foundation Ireland under Grant No. 13/IA/1833 and the Irish Research Council (IRC) for funding under their Government of Ireland Postgraduate Scheme through Grant No. GOIPG/2014/945. The authors also wish to acknowledge the DJEI/DES/SFI/HEA

Irish Centre for High-End Computing (ICHEC) for the provision of computational facilities and support. The authors also acknowledge Mark O'Brien for the provision of the experimental data; as well as John Lyons and Daniel Mortell for the images of the experimental specimens.

## REFERENCES

- [1] M. Corbett, P. Sharos, M. Hardiman, C. McCarthy, Numerical design and multi-objective optimisation of novel adhesively bonded joints employing interlocking surface morphology, *International Journal of Adhesion & Adhesives* (2017) [in review].
- [2] D. J. O'Dwyer, N. P. O'Dowd, C. T. McCarthy, In-situ SEM mechanical testing of miniature bonded joints, *International Journal of Adhesion and Adhesives* 50 (2014) 57–64.
- [3] C. Leone, I. Papa, F. Tagliaferri, V. Lopresto, Investigation of CFRP laser milling using a 30 W Q-switched Yb:YAG fiber laser: Effect of process parameters on removal mechanisms and HAZ formation, *Composites Part A: Applied Science and Manufacturing* 55 (2013) 129–142.
- [4] Aalco Metals Ltd., Aluminium alloy 5754 - H111 treadplate: material data sheet, Tech. rep., aalco, Surrey (2015).
- [5] Loctite Hysol 9466, Technical Data Sheet, Tech. rep. (2014).
- [6] Simulia® - Abaqus®, User's Manual, Version 6.14, Tech. rep., Hibbitt, Karlsson & Sorensen, Inc., Pawtucket, USA (2014).
- [7] D. J. O'Dwyer, N. P. O'Dowd, C. T. McCarthy, Micromechanical Investigation Of Damage Processes At Composite-Adhesive Interfaces, *Composites Science and Technology* 86 (2013) 61–69.
- [8] P. Ladeveze, E. LeDantec, Damage modelling of the elementary ply for laminated composites, *Composites Science and Technology* 43 (3) (1992) 257–267.
- [9] R. M. Frizzell, C. T. McCarthy, M. A. McCarthy, Predicting the effects of geometry on the behaviour of fibre metal laminate joints, *Composite Structures* 93 (7) (2011) 1877–1889.
- [10] Y. Zhou, H. Yazdani Nezhad, C. Hou, X. Wan, C. T. McCarthy, M. A. McCarthy, A three dimensional implicit finite element damage model and its application to single-lap multi-bolt composite joints with variable clearance, *Composite Structures* 131 (2015) 1060–1072.
- [11] Z. Hashin, Failure Criteria for Unidirectional FibreComposites, *Journal of Applied Mechanics* 47 (June) (1980) 329–334.
- [12] Z. P. Bažant, B. H. Oh, Crack band theory for fracture of concrete, *Materials and Structures* 16 (3) (1983) 155–177.
- [13] A. Puck, H. Schu, H. Schürmann, H. Schu, Failure Analysis of FRP Lamminates by Means of Physically Based Phenomenological Models.pdf 62 (2002) 1633–1662.
- [14] R. M. O'Higgins, An Experimental and Numerical Study of Damage Initiation and Growth in High Strength Glass and Carbon Fibre-Reinforced Composite Materials, Ph.D. thesis, University of Limerick (2007).
- [15] M. De Moura, J. Gonçalves, J. Chousal, R. Campilho, Cohesive and continuum mixed-mode damage models applied to the simulation of the mechanical behaviour of bonded joints, *International Journal of Adhesion and Adhesives* 28 (8) (2008) 419–426.